PCCP

Accepted Manuscript

ROYAL SOCIETY OF CHEMISTRY

www.rsc.org/pccp

PCCP

RSCPublishing

ARTICLE

Effects of different electrolytes on the electrochemical and dynamic behavior of electric double layer capacitors based on porous silicon carbide electrode

Myeongjin Kim, Ilgeun Oh and Jooheon Kim*

Cite this: DOI: 10.1039/xoxxoooooox

Received ooth January 2012,
Accepted ooth January 2012

DOI: 10.1039/xoxxoooooox

www.rsc.org/

Controlling the structure and morphology of porous electrode materials is an effective strategy for realizing a high surface area and efficient paths for ion diffusion. Moreover, excellent electrical conductivity can significantly decrease the internal resistance of an electrode by the formation of a conductive network and facilitate the application of electrostatic charges, which favors the accumulation of an electrical double layer. In light of these facts, we demonstrate the fabrication of β-polytype porous silicon carbide spheres (PSiCS) with a hierarchical pore structure in which micro- and mesopores are interconnected with a mesoporous network. Further, to investigate the effects of the electrolyte on the electrochemical and dynamic behavior, two-electrode symmetrical supercapacitors based on the PSiCS electrode with an aqueous electrolyte (1M potassium chloride, KCl) or an organic electrolyte (1M tetraethylammonium tetrafluoroborate in acetonitrile, $TEABF_4$/AN) were assembled. The symmetrical supercapacitor based on the PSiCS electrode with the aqueous electrolyte exhibited a high charge-storage capacity with a specific capacitance of 82.9 F g^{-1} at a scan rate of 5 mV s^{-1}, which is much higher than that obtained using the organic electrolyte (60.3 F g^{-1} at a scan rate of 5 mV s^{-1}). However, the energy density of the organic electrolyte system was 102.59 W h kg^{-1} at a scan rate of 5 mV s^{-1}, which is greatly superior to that of the aqueous electrolyte system (energy density: 29.47 W h kg^{-1}) owing to the wide cell operating voltage range.

1. Introduction

Supercapacitors (also called electrical double-layer capacitors (EDLCs)) are energy storage devices that accumulate energy in the form of electrical charge and bridge the gap between dielectric capacitors and batteries.[1-4] They are attracting attention because of their high power density, short charge time, and long cycle life.[5-7] However, they suffer from limited energy density, typically on the order of 4–5 W h kg^{-1} for fully assembled cells, which is an order of magnitude lower than that of batteries.[8] Extensive work has focused on ways to enhance their energy density by (i) increasing the capacitance using high-surface-area electrode materials and (ii) broadening the operational voltage range by using electrolytes with high potential windows.[9,10]

Traditionally, porous carbonaceous materials have been widely used as EDLC materials in order to obtain a high surface area. Various types of porous-carbon-based materials have been studied as high-surface-area electrodes, including activated carbon, carbide-derived carbons, ordered mesoporous carbons, and carbon aerogels.[11-16] However, the low electrical conductivities of these materials are not favorable for constructing a conductive network that can decrease the internal resistance of an electrode and apply electrostatic charges on the electrode's surface, forming an electrical double layer.[17] Several approaches have proposed the application of semiconductors or cermet nanowires as EDLC electrode materials instead of traditional carbon-based materials. Various types of EDLC materials such as silicon nanowires, silicon carbide (SiC) nanowires, titanium nitride nanowires, and titanium dioxide nanotubes and nanowires have attracted considerable interest because of their high surface area and excellent electrical conductivity.[18-23] Among these, SiC, in particular nanowire-type SiC, shows potential as an EDLC material owing to its high electron mobility, small band gap, and high surface area. However, because the working materials are grown directly on the current collector, these nanowire structures are ill-suited for the fabrication of hybrid composites in combination with metal oxide or conductive polymers, as well as for application as macroscale supercapacitor electrodes.

The use of SiC microsphere particles as an EDLC material was reported recently. Although SiC exhibits potential as a possible EDLC material, the porous properties, such as the surface area and pore volume, of these SiC microspherical particles are not significantly advantageous owing to their nonporous structure, resulting in low capacitive performance (72.4 F g^{-1} at a scan rate of 10 mV s^{-1} in Na_2SO_4 aqueous electrolyte).[24-26] Consequently, to obtain high charge-storage capability, it is crucial to develop SiC particles with a high surface area and pore volume by forming pores

of various sizes, because each pore has a unique role in the charge–discharge process. The macropores serve as ion-buffering reservoirs, decreasing the diffusion distance; the mesopores provide ion transport pathways with minimized resistance; and the micropores enhance the electrical double layer.[27-30] Moreover, in real applications, organic electrolytes have been employed to obtain a wide operating voltage range and chemical stability. However, the electrochemical performance of supercapacitors varies greatly depending on the electrolyte, even if the same electrode materials are used. In particular, aqueous and organic electrolytes show significantly different electrochemical and dynamic behavior due to differences in the electrolyte properties such as the ionic conductivity, ion mobility, and wettability.[31] Consequently, the effects of the electrolyte on the supercapacitor performance must be considered and investigated.

Here, we developed porous SiC spheres (PSiCS) containing micro-, meso-, and macropores via self-assembly of structure-directing agents and a carbonization reaction. The unique three-dimensional pore structures in the micro-, meso-, and macroporous SiC yield a specific surface area of up to 2302 m^2 g^{-1} with a pore volume of 1.945 cm^3 g^{-1} and provide an efficient pathway for electrolyte ions to diffuse into the interior surfaces. In addition, the β-polytype SiC exhibits an excellent electrical conductivity of 117.2 S cm^{-1}. These ternary-pore systems can be expected to exhibit advantages associated with the pore size and a synergistic effect during the electrochemical charge–discharge process. Finally, two-electrode symmetrical supercapacitors based on the PSiCS electrode with an aqueous electrolyte [1M potassium chloride (KCl)] or an organic electrolyte [1M tetraethylammonium tetrafluoroborate in acetonitrile ($TEABF_4$/AN)] were assembled to investigate the effects of the electrolyte on the electrochemical and dynamic behavior.

2. Experimental

2.1 Synthesis of porous silicon carbide spheres (PSiCS)

Polystyrene latex (PSL) spheres 80 nm in diameter were prepared as follows: 0.0975 g of sodium salt of dodecyl sulfate (SDB-Na), 0.325 g of potassium peroxodisulfate ($K_2S_2O_8$), and 32.5 mL of styrene monomer were dissolved in 186.5 mL of D.I. water. Subsequently, the mixture was heated at approximately 80°C for 18 h in a water-cooled condenser with vigorous stirring. Monodisperse PSL spheres were prepared in suspension. Sols with various PSL concentrations were formed by diluting the as-prepared suspension (14.8 wt% PS) with D.I. water. To obtain PSiCS, 0.917 g of silicon nanoparticles approximately 5 nm in diameter were dispersed in 33 mL of D.I. water. Next, 0.014 mL of hydrogen chloride (HCl), 43.3 mL of ethanol (C_2H_5OH), and 1.9742 g of $C_{16}H_{33}(EO)_{10}$ (Brij56) were added and stirred for 1 h. Finally, 14.8 wt% of PSL suspension was added in volume ratios of 1:1 and stirred for 2 h. The resulting solution mixtures were ultrasonically sprayed using a home humidifier (60 MHz and 35 W). The droplets were carried by argon gas (purity: 99.999%) at a flow rate of 100 standard cubic centimeters per minute (sccm) into a tubular reactor. The tubular reactor is separated into two segments, the drying and heating zones. The drying zone (30 mm in diameter and 700 mm in length) was heated to 150°C, and the heating zone (30 mm in diameter and 1000 mm in length) was heated to 1250°C. At the entrance to the heating zone, C_2H_5OH was ultrasonically carried by Ar gas at a flow rate of 60 sccm. The particles were recovered via filtration at the outlet of the heating zone. After the reaction was terminated and the reactor was cooled to room temperature, the resulting products were exposed to air and heated at 600°C for 4 h to remove the excess carbon. Finally, the adsorbed SiO_2 layer on the surface of the PSiCS particles was removed via treatment with hydrofluoric acid (HF). PSiCS powder (10 g) was placed in 300 mL of 10% HF solution and stirred for 24 h. Subsequently, the sample was leached with distilled water until the pH of the leaching water reached 7–8.

2.2 Characterization methods

X-ray diffraction (XRD) patterns were collected (New D8-Advance/Bruker-AXS) at a scan rate of 1° s^{-1} within a 2θ range 5°–80° using $CuK_{\alpha 1}$ radiation (0.154056 nm). The morphologies of the samples were observed using field-emission scanning electron microscopy (FE-SEM, SIGMA, Carl Zeiss). X-ray photoelectron spectroscopy (XPS) analysis was performed on a VGMicrotech ESCA2000 system using a spectrometer with a Mg Kα X-ray source (1253.6 eV) and a hemispherical analyzer. During curve fitting, the Gaussian peak widths were constant in each spectrum. Nitrogen sorption analysis was conducted using an ASAP 2020 accelerated surface area and porosimetry instrument (Micromeritics) capable of automated surface area analysis at 77 K, using Brunauer–Emmett–Teller (BET) calculations. The pore size distribution plots were recorded from the desorption branch of the isotherms on the basis of nonlocal density functional theory (DFT).

2.3 Preparation and characterization of supercapacitors

The working electrodes were fabricated as follows. The PSiCS powder was mixed with poly(tetrafluoroethylene) (60 wt% water suspension) to form an electrode consisting of 85 wt% active PSiCS materials, 10 wt% carbon black, and 5 wt% binder. The resulting mixture was then coated onto a stainless steel foil substrate (1 cm × 1 cm) and dried in a vacuum oven at 60°C for 6 h. The loading mass of each electrode was approximately 6 mg. The symmetrical supercapacitor was built with a Celgard 2400 membrane separator and employed either an aqueous electrolyte (1M KCl) or an organic electrolyte (1M $TEABF_4$/AN). Before electrochemical measurements, the assembled cells are kept for 24 h to improve the compatibility and wettability between the active material and the electrolytes. All measurements, including cyclic voltammetry (CV), galvanostatic charge–discharge characteristic, and electrochemical impedance spectroscopy (EIS) measurements, were made on a CHI 660C electrochemical workstation at room temperature. EIS measurements were made by applying an AC voltage with an amplitude of 5 mV in a frequency range of 0.001 to 10^5 Hz at open-circuit potential.

3. Results and Discussion

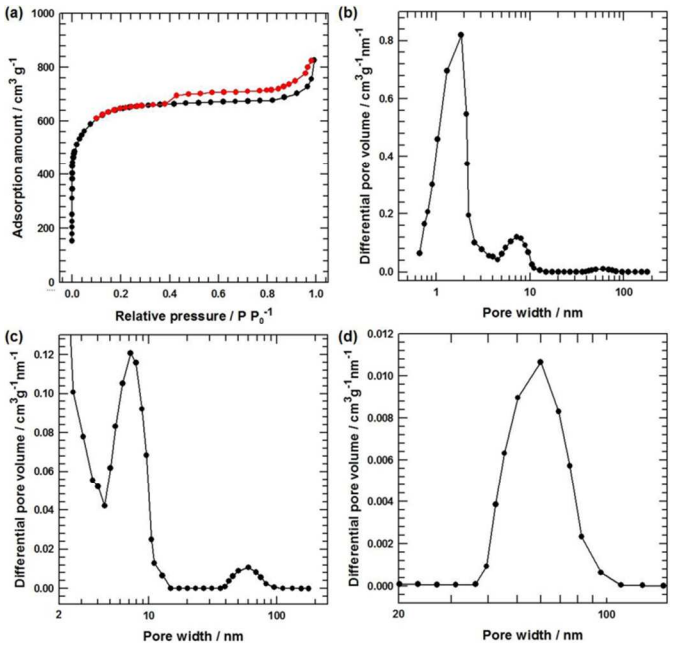

Figure 1. (a) Nitrogen adsorption-desorption isotherm of PSiCS. (b) Pore-size distribution of PSiCS. (c) Enlarged mesopore region of PSiCS. (d) Enlarged macropore region of PSiCS.

The micro-, meso-, and macroporous features of the PSiCS were confirmed via nitrogen adsorption–desorption measurements. BET and DFT analysis were employed to investigate the surface area and pore structure of the PSiCS, and the results are shown in Figure 1. The adsorption amount increases sharply at a low relative pressure (P/P_0), demonstrating the existence of micropores; a hysteresis loop appears after P/P_0 = 0.4, although no adsorption plateau is observed near P/P_0 = 1.0, indicating the presence of meso- and macropores (Figure 1(a)).[27,29] Moreover, the pore size distribution of the PSiCS (Figure 1(b), (c), and (d)) shows three distinct major regions: (i) micropores (<2 nm), with a notable peak at 1.81 nm; (ii) mesopores (2–50 nm), with a maximum peak at 7.18 nm; and (iii) macropores (>50 nm), with a maximum peak at 61.73 nm. The formation of meso- and macropores can be attributed to self-assembly of PSL spheres and a Brij56 micelle. When the solvent evaporates from the solution mixtures, PSL spheres self-assemble into a face-centered cubic (fcc) colloidal crystal; then a hexagonally aligned Brij56 micellar rod is allowed to infiltrate the spaces between the PSL spheres. Further, silicon particles are trapped in the voids of the agglomerated PSL particles and Brij56 micellar rod, forming silicon walls.[32-34] After the Brij56 micellar rod and PSL are removed, meso- and macroporous Si spheres with an ordered hexagonal arrangement of mesopores and an fcc arrangement of macropores are formed. In addition, the formation of micropores can be attributed to partial evaporation of Si atoms during carbonization of meso- and macroporous Si spheres using ethanol as the carbon source.[35] At a temperature of 1250°C, some of the Si atoms are released from meso- and macroporous Si spheres to form micropores, ultimately leading to the formation of micro-, meso-, and macroporous Si spheres. The remaining micro-, meso-, and macroporous Si spheres react with the active carbon species decomposed from ethanol to form micro-, meso-, and macroporous SiC spheres. After carbonization, the mother meso- and macroporous Si spheres are completely converted into micro-, meso-, and macroporous SiC spheres.[35] Therefore, the total specific surface area of the PSiCS is calculated to be more than 2302 m^2 g^{-1}, with a micropore surface area of 1852 m^2 g^{-1}, mesopore surface area of 429 m^2 g^{-1}, and macropore surface area of 21 m^2 g^{-1}. In addition, according to the DFT calculation, the total pore volume is 1.945 cm^3 g^{-1}, with a micropore volume of 0.838 cm^3 g^{-1}, mesopore volume of 0.771 cm^3 g^{-1}, and macropore volume of 0.336 cm^3 g^{-1}. In terms of the ion transport behavior during the charge–discharge process, mixed porous structures with an appropriate quantity of three-dimensional interconnected meso- and macropores promote global ion transport throughout the entire material by reducing the ion diffusion distance and transport resistance.[36] In terms of the ion adsorption behavior, the considerable number of micropores plays a crucial role in ion accumulation, resulting in stronger electrical double-layer properties.[37]

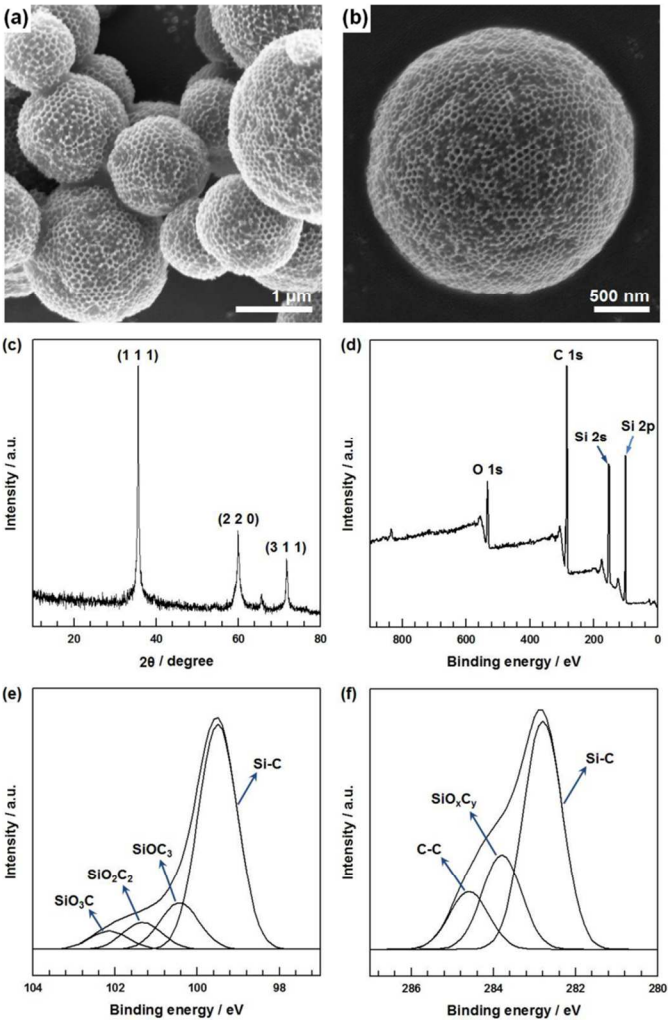

Figure 2. (a) Low-magnification FE-SEM image of PSiCS. (b) High-magnification FE-SEM image of PSiCS. (c) XRD patterns of PSiCS. (d) XPS wide scan survey spectra of PSiCS. (e) XPS Si 2p spectra of PSiCS. (f) XPS C 1s spectra of PSiCS.

The microstructure, crystalline structure, and chemical composition of the PSiCS were investigated, and the results are shown in Figure 2. FE-SEM images show that PSiCS particles range in diameter from 1 to 3 μm and exhibit a spherical morphology (Figure 2(a)). The magnified FE-SEM image in Figure 2(b) shows open and interconnected macropores in a three-dimensional framework. The XRD pattern of the PSiCS (Figure 2(c)) shows three β-SiC peaks at 2θ = 35.6°, 60°, and 71.7°, which were assigned to the (1 1 1), (2 2 0), and (3 1 1) reflections, respectively. These were correlated with the fcc β-SiC structure in accordance with the reference data (JCPDS 29-1129, a = 4.3589 Å).[38,39] The electrical conductivity of the PSiCS was determined to be 117.2 S cm^{-1} for pressed pellets using the four-point probe method. The β-polytype crystalline structure of as-synthesized PSiCS allows for excellent electrical conductivity because of its small band gap (~2.4 eV) and high electron mobilities (~800 cm^2 V^{-1} s^{-1} in low-doped material).[40] Figure 2(d) shows the XPS survey spectrum of the PSiCS, which consist of three elements, C, Si, and O. To obtain detailed surface information on the PSiCS, the Si 2p and C 1s core-level spectra were deconvoluted. The Si 2p region of the spectrum of the PSiCS (Figure 2(e)) shows that in addition to the strong Si–C peak at a binding energy of 99.51 eV, some intermediate oxidation products of SiC ($SiOC_3$ at 100.44 eV, SiO_2C_2 at 101.34 eV, and SiO_3C at 102.15 eV) also exist on the surface.[41] The C 1s core level (Figure 2(f)) shows strong binding energy peaks for Si–C bonds at 282.81 eV and C–C bonds at 284.62 eV, with several binding energy peaks for SiO_xC_y at 283.79 eV.[42] The Si–C/SiO_xC_y peak area ratio calculated from the Si 2p spectra is 2.47, which shows good agreement with the Si–C/SiO_xC_y ratio obtained from the C 1s spectrum (2.41).

Given the highly porous nature of the PSiCS, their electrochemical performance as an electrode for supercapacitors was evaluated. Using a best-practice method, two-electrode symmetrical cells were constructed using the PSiCS as an electrode material with an aqueous electrolyte (1M KCl) or an organic electrolyte (1M $TEABF_4$/AN). Figure 3(a) shows the CV curve of the symmetrical supercapacitor measured in the aqueous electrolyte at a scan rate of 5 mV s^{-1}. The CV curve exhibits ideal capacitive behavior and has a nearly rectangular shape, even at an operating voltage of up to 1.6 V, indicating typical electrical double-layer behavior with quick dynamics and good charge propagation.[43] To obtain more information on the capacitive performance, the symmetrical supercapacitor using an aqueous electrolyte was subjected to detailed measurements. Figure 3(b) shows the CV curves of the aqueous electrolyte system acquired at scan rates of 5, 10, 20, 50, and 100 mV s^{-1}. The CV profiles retain a largely rectangular shape with high symmetry and do not show any signs of obvious distortion with increasing potential scan rate, indicating ideal capacitive properties and excellent reversibility.[44] The outstanding electrochemical performance of PSiCS in the KCl aqueous electrolyte can be explained as follows: (i) Interconnected macropores within frameworks are favorable for the formation of an ion-buffering reservoir to minimize the diffusion distances from the external electrolyte to the interior surfaces. (ii) The mesopores of PSiCS provide low-resistance pathways for ion diffusion in the pores, which improves the capacitive activity. (iii) The abundant micropores play an essential role in optimizing the electrical double-layer surfaces, which improves the value of the capacitance. (iv) The excellent electrical conductivity of PSiCS can significantly decrease the internal resistance of an electrode via the construction of a conductive network and facilitate the application of electrostatic charges, encouraging the accumulation of electrical double layers.[27-30] Although these unique porous features of PSiCS yield ideal supercapacitive behavior in the aqueous electrolyte, the use of an organic electrolyte yields somewhat different electrochemical behavior. Figure 3(c) shows the CV curve of organic electrolyte system at a scan rate of 5 mV s^{-1} and an operating voltage ranging from 0 to 3.5 V. The CV curve of the PSiCS-based supercapacitor with the organic electrolyte deviates from the ideal rectangular shape. Moreover, as shown in Figure 3(d), the shape of the CV curve gradually becomes oval with increasing scan rate, with lower

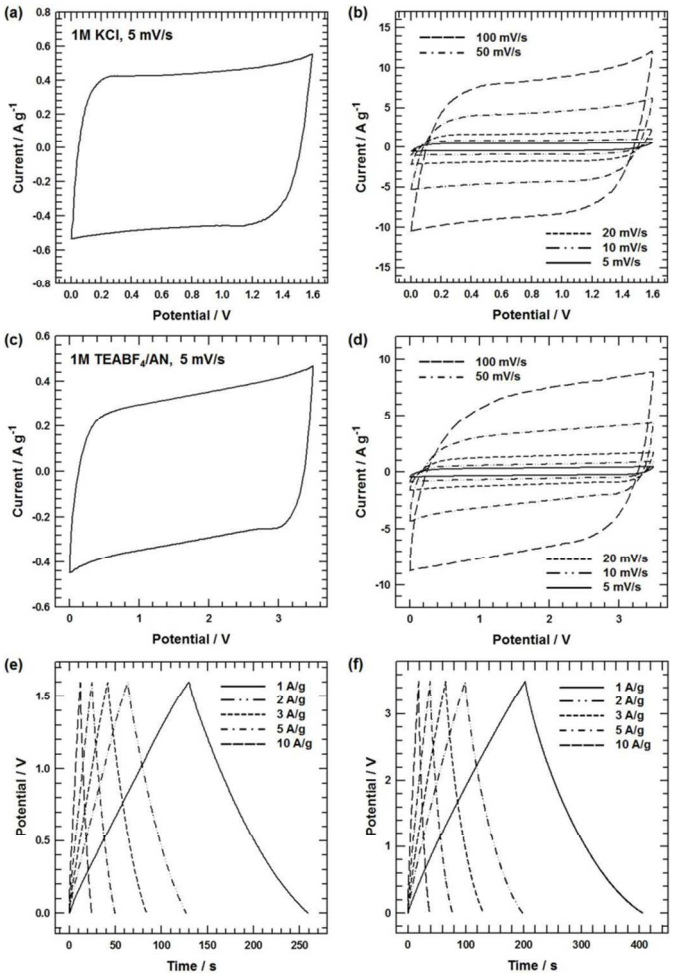

Figure 3. Electrochemical performance of two-electrode supercapacitors based on PSiCS electrodes with 1M KCl aqueous electrolyte and 1M $TEABF_4$/AN organic electrolyte. (a) CV curve of 1M KCl electrolyte at a scan rate of 5 mV s^{-1}. (b) CV curves of 1M KCl electrolyte as different scan rates. (c) CV curve of 1M $TEABF_4$/AN electrolyte at a scan rate of 5 mV s^{-1}. (d) CV curves of 1M $TEABF_4$/AN electrolyte as different scan rates. (e) Galvanostatic charge/discharge curves of 1M KCl electrolyte as different current densities. (f) Galvanostatic charge/discharge curves of 1M $TEABF_4$/AN electrolyte as different current densities.

response current densities at each corresponding scan rate compared with the aqueous electrolyte system because of the poor compatibility and ionic conductivity of the organic electrolyte.[45] Figure 3(e) shows the galvanostatic charge–discharge curves of aqueous electrolyte system measured at current densities of 1, 2, 3, 5, and 10 A g^{-1}. The curves at various current densities show a good linear relationship between the charge–discharge potentials and time, indicating a rapid *I–V* response and ideal capacitive characteristics.[46] However, the typical galvanostatic charge–discharge curves of the organic electrolyte system (Figure 3(f)) at various current densities show a slight curvature in the discharge curves to their charge counterparts compared with the aqueous electrolyte system because of the poor electrochemical activity of the organic electrolyte, which was confirmed by the CV curve behavior.

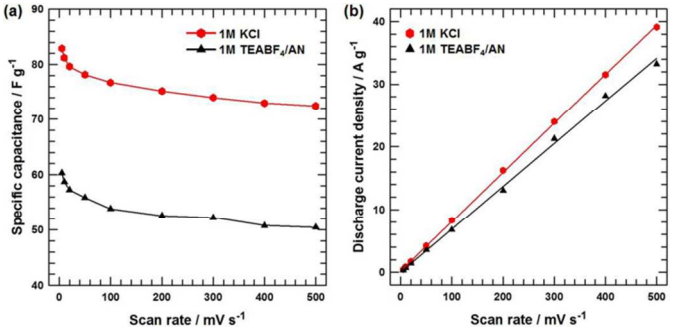

Figure 4. (a) Specific capacitance of 1M KCl and $TEABF_4$/AN electrolyte at different scan rates. (b) Discharge current densities as a function of scan rate for 1M KCl and $TEABF_4$/AN electrolyte.

The specific capacitances (C_s) are calculated from the CV curves using the following equation:[47]

$$C_s = \frac{1}{v(V_c - V_a)} \int_{V_a}^{V_c} I(V)dV \qquad (1)$$

where C_s is the specific capacitance (F g^{-1}), v is the potential scan rate (mV s^{-1}), $V_c - V_a$ represents the sweep potential range (V), and $I(V)$ denotes the response current density (A g^{-1}). Figure 4(a) shows the specific capacitance of the symmetrical supercapacitors with the aqueous and organic electrolytes as a function of the scan rate. The calculated C_s values of the aqueous and organic electrolyte systems at a scan rate of 5 mV s^{-1} are 82.9 and 60.3 F g^{-1}, respectively. Moreover, the symmetrical supercapacitor using the aqueous electrolyte exhibits much higher C_s values over the entire range of scan rates. Importantly, the C_s values of both the aqueous and organic electrolyte systems decreased steadily with increasing scan rate owing to the reduced access of ions to the active surface.[48] Therefore, the capacitance retention of the aqueous and organic electrolyte systems in response to a scan rate increase from 5 to 500 mV s^{-1} are 87.4% (from 82.9 F g^{-1} at 5 mV s^{-1} to 72.4 F g^{-1} at 500 mV s^{-1}) and 83.7% (from 60.3 F g^{-1} at 5 mV s^{-1} to 50.4 F g^{-1} at 500 mV s^{-1}), respectively. As a result, both the capacitive and rate performance of the aqueous electrolyte system are greatly superior to those of the organic electrolyte system because of the poor compatibility and ionic conductivity of the organic electrolyte. Figure 4(b) shows the relationship between the discharge current density and scan rate obtained from the CV curves of the PSiCS-based supercapacitors with the aqueous and organic electrolytes. Surprisingly, the evolved discharge current density for the aqueous electrolyte system has an almost linear relationship with the scan rate in the scan rate range from 5 to 500 mV s^{-1}. A linear relationship with R^2 = 0.9997 was observed for the discharge curves, indicating that the charge–discharge process was remarkably fast over the entire electrode surface, even at a high scan rate, whereas the discharge current density of the organic electrolyte system did not exhibit a linear dependence (R^2 = 0.9974). A linear relationship was observed only at slow scan rates (from 5 to 100 mV s^{-1}), indicating limited ion mobility in the organic electrolyte.[31]

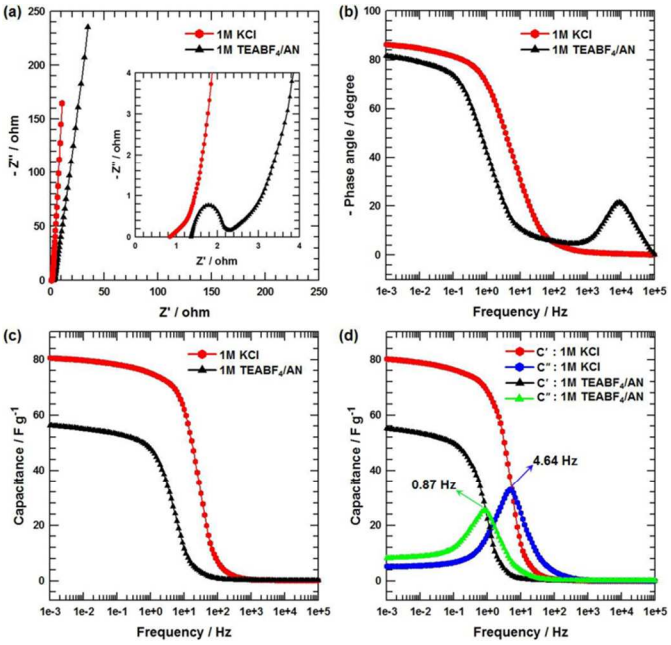

Figure 5. (a) Nyquist plots of 1M KCl and $TEABF_4$/AN electrolyte. Inset magnifies the data in the high-frequency range. (b) Impedance phase angle versus frequency of 1M KCl and $TEABF_4$/AN electrolyte. (c) Capacitance as a function of frequency obtained from EIS of 1M KCl and $TEABF_4$/AN electrolyte. (d) Real and imaginary part of capacitance as a function of frequency for 1M KCl and $TEABF_4$/AN electrolyte.

EIS measurements were performed for two cells with identical PSiCS electrodes immersed in the two different electrolytes. Figure 5(a) shows the Nyquist plots for the aqueous and organic electrolyte systems at a frequency range of 100 KHz to 1 mHz. The Nyquist plots consist of three parts: (i) the intersection of the curve at the *X* axis represents the series resistance of the cells (R_s), which generally originates from the solution resistance in the electrolyte, the separator resistance, and the external circuit resistance, and the diameter of the semicircle represents the charge transport resistance (R_{ct}); (ii) a straight line with a slope of 45° in the mid-frequency range corresponds to the semi-infinite Warburg impedance resulting from the frequency dependence of ion diffusion/transport in the electrolyte; (iii) a vertical line at low frequencies is caused by the accumulation of ions at the bottom of the pores of the electrode. The nearly vertical line indicates good capacitive behavior without diffusion limitations. The organic electrolyte system shows much

higher R_s value compared to aqueous electrolyte system due to the inferior ionic conductivity and poor compatibility and wettability between the active materials and the organic electrolyte.[31] Moreover, the magnified high to medium-frequency regions of the Nyquist plots for the organic and aqueous electrolyte systems show major differences. The emergence of a semicircle indicates the lower ionic conductivity of the organic electrolyte, and the longer 45° phase shift segment implies a higher Warburg impedance. In addition, as shown in Figure 5(b), the phase angle of the organic electrolyte system in the lower-frequency-limitation region is −81.6°, which is significantly lower than that of the aqueous electrolyte system (−86.3°), indicating slower ion diffusion in the electrolyte and slower ion adsorption onto the electrode surface.[49] The poor compatibility between the active materials and the organic electrolyte prevents the electrolyte from adequately accessing the external surface and inner volume of the PSiCS, which results in limited outer-surface accessibility.

Complex capacitance analysis, which can be easily performed using the impedance spectra, has emerged as an excellent technique for investigating the bulk and interfacial electrochemical properties. Figure 4(c) presents the capacitance–frequency dependence derived from the Nyquist plot according to the following equation:[50]

$$C(f) = \frac{-1}{2\pi f Z''(f)} \quad (2)$$

where f is the frequency, and $Z''(f)$ is the imaginary part of the impedance. The relationship between the capacitance and the frequency reflects the penetration of the alternating current into the bulk pores of the electrode material, which can illustrate how many electrolyte ions have reached the pore surfaces at a specific frequency.[50] The aqueous and organic electrolyte systems both reached full capacitance at a low frequency, and the capacitance started to decrease with increasing frequency. At low frequency, electrolyte ions penetrate deep inside the pores of the PSiCS electrode, accessing more electrode surface and thereby contributing to the high capacitance value. At higher frequencies, electrolyte ions can access only the surface of PSiCS electrode, whereas the deeper pores are not accessed, giving rise to a sharp decrease in the capacitance.[51] The $C(f)$ value of the aqueous electrolyte system at 1 mHz was calculated to be 80.5 F g^{-1}, which is much higher than that of the organic electrolyte system (56.3 F g^{-1}), in good agreement with the CV curve behavior. Moreover, both $C(f)$ values at 1 mHz are close to the specific capacitance value calculated by CV measurement. In addition, when the frequency is increased, the $C(f)$ value of the organic electrolyte system starts to decrease sharply at a lower frequency (0.6 Hz) than that of the aqueous electrolyte system does (3.5 Hz), indicating that the unfavorable ionic diffusion to the active electrode surface in the organic electrolyte system leads to the poor rate capability at high frequencies or high scan rates. Plots of the frequency-dependent real ($C'(f)$) and imaginary ($C''(f)$) components of the capacitance were obtained from the impedance spectra according to the following equations:[52]

$$C'(f) = \frac{-Z''(f)}{2\pi f |Z(f)|^2} \quad (3)$$

$$C''(f) = \frac{Z'(f)}{2\pi f |Z(f)|^2} \quad (4)$$

where $Z'(f)$ and $Z''(f)$ are the real and imaginary parts of the impedance, respectively, and $|Z(f)|$ is the absolute value of the impedance. As shown in Figure 5(d), the $C'(f)$ values of the aqueous and organic electrolyte systems exhibit behavior similar to that of $C(f)$. At the lowest frequency (1 mHz), $C'(f)$ reached 80.2 F g^{-1} for the device with the aqueous electrolyte and 55.1 F g^{-1} for that with the organic electrolyte. When the frequency is increased, $C'(f)$ decreases, and at a high frequency, the capacitor behaves like a pure resistor. In addition, the time constant (τ_0), which is a characteristic parameter indicating the rate capability of an electrical system, can be estimated from the peak frequency of $C''(f)$ using the following equation:[53]

$$\tau_0 = \frac{1}{f} \quad (5)$$

where f is the frequency corresponding to the peak frequency of the imaginary capacitance. As shown in Figure 5(d), the maximum capacitances ($C''(f)$) of the aqueous and organic electrolyte systems are observed at frequencies of 4.64 and 0.87 Hz, giving corresponding time constants of 0.21 and 1.13 s, respectively. The lower time constant of the aqueous electrolyte system indicates the favorable accessibility of the outer surface of the electrode material to the electrolyte ions, resulting in outstanding rate performance.[54] Therefore, the trend of the time constants for the aqueous and organic electrolyte systems agrees well with the capacitance retention performance obtained from CV measurements (Figure 4(a)).

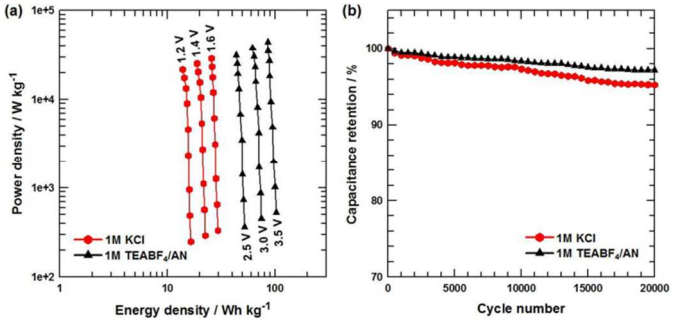

Figure 6. (a) Ragone plot of two-electrode supercapacitors of 1M KCl and $TEABF_4$/AN electrolyte as a function of cell operating voltage. (b) Cycling stability of two-electrode supercapacitors of 1M KCl and $TEABF_4$/AN electrolyte measured at a current density of 10 A g^{-1}.

The power density and energy density, which are important parameters for determining the electrochemical performance, were also used to characterize the aqueous and organic electrolyte systems. They can be estimated using the following equations:[25]

$$E = \frac{1}{2} C(\Delta V)^2 \quad (6)$$

$$P = \frac{E}{t} \quad (7)$$

where P, C, ΔV, t, and E represent the power density (W kg^{-1}), specific capacitance based on the mass of the electroactive material (F g^{-1}), cell voltage for charging and discharging (V), discharge time (s), and energy density (W h kg^{-1}), respectively. Ragone plots of the symmetrical PSiCS-based supercapacitors using the aqueous and organic electrolytes at different scan rates are shown in Figure 6(a). At a low scan rate of 5 mV s^{-1}, the power and energy density values for the organic electrolyte system (operating voltage: 3.5 V) were found to be 527.62 W kg^{-1} and 102.59 W h kg^{-1}, respectively, which are greatly superior to those of the aqueous electrolyte system (power density: 331.6 W kg^{-1} and energy density: 29.47 W h kg^{-1} at an operating voltage of 1.6 V). Although the organic electrolyte system exhibits lower specific capacitance performance than the aqueous electrolyte system, the wide operating voltage range of the organic electrolyte system contributes to the significant enhancement of the energy and power density performance. In addition, as shown by the relationship between the energy and power density at various cell operating voltages for each electrolyte, the applied energy and power densities of the cell can be controlled to some extent by selecting a suitable working voltage to satisfy practical requirements. A cyclic stability test of the aqueous and organic electrolyte cells was performed for 20000 cycles at a current density of 10 A g^{-1} over an operating voltage range of 1.6 V (from 0 to 1.6 V) and 3.5 (from 0 to 3.5 V), respectively. Figure 6(b) illustrates the specific capacitance retention as a function of the cycle number. After 20000 cycles, the capacitance retention of the aqueous and organic electrolyte cells were 95.2% and 97.4%, respectively, demonstrating that the aqueous and organic electrolyte cells have similar cycle stabilities.

4. Conclusion

In summary, PSiCS with micro-, meso-, and macropores were synthesized via the template method, and the carbonization reaction was induced via aerosol spray drying. A symmetrical supercapacitor based on a PSiCS electrode with an aqueous electrolyte (1M KCl) exhibited a high charge-storage capacity, with a specific capacitance of 82.9 F g^{-1} at a scan rate of 5 mV s^{-1}, an 87.4% rate performance from 5 to 500 mV s^{-1}, and a short time constant of 0.21 s. In a system with an organic electrolyte (1M $TEABF_4$/AN), a specific capacitance of 60.3 F g^{-1} was verified at a scan rate of 5 mV s^{-1}, with an 83.7% rate performance from 5 to 500 mV s^{-1} and a longer time constant of 1.13 s. These results are attributed to the poor compatibility between the active materials and the organic electrolyte, which prevents the electrolyte from adequately accessing the external surface and inner volume of the PSiCS, and the lower ionic conductivity and mobility of the organic electrolyte compared to the aqueous electrolyte. However, the energy and power densities of the organic electrolyte system were 102.59 W h kg^{-1} and 527.62 W kg^{-1}, respectively, at a scan rate of 5 mV s^{-1}, which are greatly superior to those of the aqueous electrolyte system (energy density: 29.47 W h kg^{-1}, power density: 331.6 W kg^{-1}) because of the wide cell operating voltage range. Therefore, the supercapacitor performance achieved with PSiCS electrodes using aqueous or organic electrolytes can efficiently satisfy the practical requirements if the appropriate electrolyte is selected.

Acknowledgements

This research was supported by Global Ph.D. Fellowship Program through the National Research Foundation of Korea (NRF) funded by the Ministry of Education (2014H1A2A1021380).

Notes and references

School of Chemical Engineering & Materials Science, Chung-Ang University, 84 Heukseok-Ro, Dongjak-gu, Seoul 156-756, Korea.
E-mail : jooheonkim@cau.ac.kr
Phone : +82-2-820-5763, Fax : +82-2-824-3495

1. V. Subramanian, H. Zhu, R. Vajtai, P.M. Ajayan and B. Wei, *J. Phys. Chem. B.*, 2005, **109**, 20207-20214.
2. A.L. Mohana, R.F. Estaline, A. Imran and J.S. Ramaprabhu, *Nanoscale Res. Lett.*, 2008, **3**, 145-151.
3. A.C.-G. Karina, L.-C. Monica, C.-P. Nieves and G.-R. Pedro, *Adv. Funct. Mater.*, 2005, **15**, 1125-1133.
4. J. Chow, R.J. Kopp and P.R. Portney, *Science*, 2003, **302**, 1528-1531.
5. Z. Wen, X. Wang, S. Mao, Z. Bo, H. Kim, S. Cui, G. Lu, X. Feng and J. Chen, *Adv. Mater.*, 2012, **24**, 5610-5616.
6. R. Kotz and M. Carlen, *Electrochim. Acta*, 2000, **45**, 2483-2498.
7. Z. Chen, Y. Qin, D. Weng, Q. Xiao, Y. Peng, X. Wang, H. Li, F. Wei and Y. Lu, *Adv. Funct. Mater.*, 2009, **19**, 3420-3426.
8. A. Burke, *Electrochim. Acta*, 2007, **53**, 1083-1091.
9. M. Armand, F. Endres, D. R. MacFarlane, H. Ohno and B. Scrosati, *Nat. Mater*. 2009, **8**, 621-629.
10. T. Kim, G. Jung, S. Yoo, K.S. Suh and R.S. Ruoff, *ACS Nano*, 2013, **7**, 6899-6905.
11. J. Chmiola, G. Yushin, Y. Gogotsi, C. Portet, P. Simon and P. L. Taberna, *Science*, 2006, **313**, 1760-1763.
12. C. Portet, M. A. Lillo-Rodenas, A. Linares-Solano and Y. Gogotsi, *Phys. Chem. Chem. Phys.* 2009, **11**, 4943-4945.
13. R. Dash, J. Chmiola, G. Yushin, Y. Gogotsi, G. Laudisio, J. Singer, J. Fischer and S. Kucheyev, *Carbon*, 2006, **44**, 2489-2497.
14. W. Xing, S. Z. Qiao, R. G. Ding, F. Li, G. Q. Lu, Z. F. Yan and H. M. Cheng, *Carbon*, 2006, **44**, 216-224.
15. K. Jurewicz, C. Vix-Guterl, E. Frackowiak, S. Saadallah, A. Reda, J. Parmentier, J. Patarin and F. Beguin, *J. Phys. Chem. Solids*. 2004, **65**, 287-293.
16. R. W. Pekala, J. C. Farmer, C. T. Alviso, T. D. Tran, S. T. Mayer, J. M. Miller and B. Dunn, *J. Non-Cryst. Solids* 1998, **225**, 74-80.
17. L.L. Zhang, R. Zhou and X.S. Zhao, *J. Mater. Chem.*, 2010, **20**, 5983-5992.
18. J.W. Choi, J. McDonough, S. Jeong, J.S. Yoo, C.K. Chan and Y. Cui, *Nano Lett.*, 2010, **10**, 1409-1413.
19. J.P. Alper, M. Vincent, C. Carraro and R. Maboudian, *Appl. Phys. Lett.*, 2012, **100**, 163901-163904.

20. J.P. Alper, M.S. Kim, M. Vincent, B. Hsia, V. Radmilovic, C. Carraro and R. Maboudian, *J. Power Sources*, 2013, **230**, 298-302.
21. X. Lu, G. Wang, T. Zhai, M. Yu, S. Xie, Y. Ling, C. Liang, Y. Tong and Y. Li, *Nano Lett.*, 2012, **12**, 5376-5381.
22. X. Lu, G. Wang, T. Zhai, M. Yu, J. Gan, Y. Tong and Y. Li, *Nano Lett.*, 2012, **12**, 1690-1696.
23. H. Zhang, T. Zhai, M. Yu, S. Xie, C. Liang, W. Zhao, S.C.I. Wang, Z. Zhang and X. Lu, *J. Mater. Chem. C*, 2013, **1**, 225-229.
24. M. J. Kim, Y. J. Yoo and J. H. Kim, *J. Power Sources*, 2014, **265**, 214-222.
25. M. J. Kim and J. H. Kim, *Phys. Chem. Chem. Phys.* 2014, **16**, 11323-11336.
26. M. J. Kim and J. H. Kim, *ACS Appl. Mater. Interfaces* 2014, **6**, 9036-9045.
27. F. Xu, R. Cai, Q. Zeng, C. Zou, D. Wu, F. Li, X. Lu, Y. Liang and R. Fu, *J. Mater. Chem.*, 2011, **21**, 1970-1976.
28. Z.S. Wu, Y. Sun, Y.Z. Tan, S. Yang, X. Feng and K. Mullen, *J. Am. Chem. Soc*. 2012, **134**, 19532-19535.
29. D.W. Wang, F. Li, M. Liu, G.Q. Lu and H.M. Cheng, *Angew. Chem. Int. Ed.* 2008, **47**, 373-376.
30. W. Xiong, M. Liu, L. Gan, Y. Lv, Z. Xu, Z. Hao and L. Chen, *Colloids and Surfaces A: Physicochem. Eng. Aspects* 2012, **411**, 34-39.
31. J. Kang, J. Wen, S.H. Jayaram, A. Yu and X. Wang, *Electrochim. Acta*, 2014, **115**, 587-598.
32. Z.Y. Yuan and B.L. Su, *J. Mater. Chem.*, 2006, **11**, 663-677.
33. Y. Lu, H. Fan, A. Stump, T.L. Ward, T. Rieker and C.J. Brinker, *Nature*, 1999, **398**, 223-226.
34. N.M. Vinothan, I. Arnout, D.T. James and J.P. David, *Adv. Mater.*, 2001, **13**, 447-450.
35. Y. Yang, G. Meng, X. Liu, L. Zhang, Z. Hu, C. He and Y. Hu, *J. Phys. Chem. C.*, 2008, **112**, 20126-20130.
36. L. Z. Fan, Y. S. Hu, J. Maier, P. Adelhelm, B. Smarsly and M. Antonietti, *Adv. Funct. Mater.*, 2007, **17**, 3083-3087.
37. Y. R. Liang, D. C. Wu and R. W. Fu, *Langmuir*, 2009, **25**, 7783-7785.
38. Y. Zhang, E.W. Shi, Z.Z. Chen, X.B. Li and B. Xiao, *J.Mater.Chem.*, 2006, **16**, 4141-4145.
39. Z. Liu, L. Ci, N.Y. Jin-Phillipp and M. Ruhle, *J. Phys. Chem. C.*, 2007, **111**, 12517-12521.
40. J.B. Casady and R.W. Johnson, *Solid-State Electron.*, 1996, **39**, 1409-1422.
41. K. Shimoda, J.S. Park, T. Hinoki and A. Kohyama, *Appl. Surf. Sci.* 2007, **253**, 9450-9456.
42. R. Liu, B. Liu, K. Zhang, M. Liu, Y. Shao and C. Tang, *J. Nuci. Mater*. 2014, **453**, 107-114.
43. M. J. Kim, Y. S. Hwang and J. H. Kim, *J. Power Sources*, 2013, **239**, 225-233.
44. M. J. Kim, Y. S. Hwang, K. C. Min and J. H. Kim, *Phys. Chem. Chem. Phys.* 2013, **15**, 15602-15611.
45. W. Qian, F. Sun, Y. Xu, L. Qiu, C. Liu, S. Wang and F. Yan, *Energy Environ. Sci*. 2014, **7**, 379-386.
46. M. J. Kim, Y. S. Hwang and J. H. Kim, *Phys. Chem. Chem. Phys.* 2014, **16**, 351-361.
47. X. Xie and L. Gao, *Carbon*, 2007, **45**, 2365-2373.
48. B.G. Choi, M. Yang, W.H. Hong, J.W. Choi and Y.S. Huh, *ACS nano*, 2010, **6**, 4020-4028.
49. J. Lin, C. Zhang, Z. Yan, Y. Zhu, Z. Peng, R.H. Hauge, D. Natelson and J.M. Tour, *Nano Lett.*, 2013, **13**, 72-78.
50. W. Xing, S.Z. Qiao, R.G. Ding, F. Li, G.Q.Lu, Z.F. Yan and H.M. Cheng, *Carbon*, 2006, **44**, 216-224.
51. M. Biswal, A. Banerjee, M. Deo and S. Ogale, *Energy Environ. Sci*. 2013, **6**, 1249-1259.
52. I. Stepniak and A. Ciszewski, *Electrochim. Acta*, 2011, **56**, 2477-2482.
53. I. Stepniak and A. Ciszewski, *J. Power Sources*, 2010, **195**, 5130-5137.
54. C. Yang, M. Zhou and Q. Xu, *Phys. Chem. Chem. Phys.* 2013, **15**, 19730-19740.